SAND2014-4380C

Sensitivity Analysis and Verification of a 1-D Surface Solid Combustion Model for a Fire CFD Boundary Condition

Alexander L. Brown,[1] David Glaze,[2] and Flint Pierce[3]
Sandia National Laboratories, Albuquerque, NM, 87185

Predicting the behavior of solid fuels in response to a fire is a complex endeavor. Heterogeneity, charring, and intumescence are a few examples of the many challenges presented by some common materials. If one desires to employ a 3-dimensional computational fluid dynamics (CFD) model for fire, an accurate solid combustion model for materials at the domain boundary is often desirable. Methods for such modeling are not currently mature, and this is a current topic of research. For some practical problems, it may be acceptable to abstract the surface combustible material as a 1-dimensional reacting boundary condition. This approach has the advantage of being a relatively simple model, and may provide acceptably accurate predictions for problems of interest. Such a model has recently been implemented in Sandia's low-Mach number CFD code for reacting flows, the SIERRA/FUEGO code. Theory for the implemented model is presented. The thermal transport component of the model is verified by approximating a 1-D conduction problem with a closed form solution. The code is further demonstrated by predicting the fire behavior of a block of burning plexiglas (PMMA). The predictions are compared to the reported data from a corresponding experimental program. The predictions are also used to evaluate the sensitivity of model parameters through a sensitivity study using the same test configuration.

Nomenclature

α	=	Thermal diffusivity
ϵ	=	Surface emissivity of porous boundary
ϵ_b	=	Emissivity of porous boundary virtual back-site surface
$\bar{\rho}$	=	Porous boundary material mixture bulk density
ρ_k	=	Density of material k in its native porous state
$\rho_{s0,k}$	=	Density of material k in its pure, solid state
σ	=	Stefan-Boltzmann constant
$\bar{\psi}$	=	Porous boundary material mixture porosity
ψ_k	=	Porosity of material k in its native porous state
$\dot{\omega}_c'''$	=	Overall volumetric mass generation rate
$\dot{\omega}_k'''$	=	Volumetric mass generation rate of species k
A_i	=	Cross-sectional area of virtual boundary discretization control volume i
$\bar{c}$	=	Porous boundary material mixture specific heat capacity
c_k	=	Specific heat capacity of species k
h_c	=	Surface convection coefficient
$\bar{k}$	=	Porous boundary material mixture thermal conductivity
k_k	=	Thermal conductivity of species k
$\dot{q}'''$	=	Volumetric heat generation rate
T	=	Temperature of porous boundary material

[1] R&D Engineer, Fire Science and Technology Department, PO Box 5800, MS 1135, Albuquerque, NM, 87185-1135
[2] R&D Engineer, Computational Thermal and Fluid Mechanics Department, PO Box 5800, MS 0836, Albuquerque, NM, 87185-0836
[3] R&D Engineer, Computational Thermal and Fluid Mechanics Department, PO Box 5800, MS 0828, Albuquerque, NM, 87185-0828

T_w = Wall (surface) temperature of porous boundary material
T_N = Boundary material virtual back-side surface temperature
T_{ref} = Boundary material virtual back-side quiescent environment temperature
V_i = Volume of boundary discretization control volume i
X_k = Volume fraction of species k in porous boundary material
Y_k = Mass fraction of species k in porous boundary material

I. Introduction

FIRE modeling may require the ability to model a fuel of initial gaseous, liquid, or solid state. Of these, the gaseous fuel tends to be the simplest, as reactions do not involve pyrolysis or evaporation. Liquids undergo phase change before combustion, and may also involve complexities including flow in the liquid phase, multiphase heat transport, and participating media radiation. For solid materials, the dynamics can be even more complex, as charring may occur, or liquid flow may result from polymeric breakdown or phase change. Furthermore, mass diffusion can become a rate-limiting factor for many practical charring materials. These can be difficult to model because thermal properties can be transient, and relevant reaction length scales can vary based on the type of material. Examples of relevant length scales include the fiber diameter for a carbon fiber epoxy, the cell size for an organic material like wood, or the charring pore diameter for an intumescent material. Burning solids are clearly difficulty to simulate, and thus the need for work on developing methods for modeling burning materials.

A simple abstraction that can be useful for modeling involves treating the solid reacting material as one-dimensional. For low conduction coefficient-solids that do not exhibit controlling behaviors of high complexity, this simple model may be able to provide a first-order estimate so that fire behavior can be predicted. Recent examples of such models are found in the literature[1-3].

Sandia National Labs develops the Low Mach Module, sometimes referred to as Fuego, as part of the Sierra Thermal/Fluids capabilities. The primary objective of this code is simulating high-fidelity three-dimensional turbulent fire dynamics in support of high-consequence fire safety analyses. Models have heretofore been limited to solving liquid and gas fire scenarios. Because many practical problems involve solid materials, there is a desire to have a quality model for simulating the behavior of this class of materials. Such a capability was implemented under a program for studying complex composite materials. The complexities associated with composite materials (three-dimensional by their very nature) challenged qualifying the model for predictive use. Thus, this effort is designed to reduce the complexity of the problem and demonstrate the model in an environment more amenable to characterization.

The objective of this paper is to demonstrate the development of a one-dimensional fire boundary condition for simple solid materials. A simple one-dimensional model is formulated, and presented in the theory section. Verification of the implementation is then described. Then, the new model is used to simulate a simple scenario for which data exist, found in the literature. The objective of this portion of this paper is not to show validation, but rather to explore input parameter sensitivity, and to evaluate resolution requirements. PMMA is often used as a simple burning fuel, as it does not tend to produce char, and the decomposition mechanism is reasonably well studied. Among several existing experimental reports[4-7], the work of Ndubizu *et al.* (2005)[7] was selected for modeling in this effort. These tests were selected due to their being well described, and amenable to simulation for this effort.

II. Theory

Figure 1 illustrates a two-dimensional representation of the virtual mesh used for this 1-D surface solid combustion boundary condition. One layer of elements above the boundary is shown on the left, within which the Sierra Low Mach Module performs its normal fluid solve using the control volume finite element (CVFEM) method[8,9]. The CVFEM sub-control volumes are demarcated with dashed lines. An equal-order interpolation methodology is used, so that all solution variables are stored at the element vertices.

For this boundary condition, a series of independent one-dimensional virtual domains exist behind each CVFEM surface node, and each virtual 1-D domain has a cross-sectional area that matches the group of CVFEM boundary sub-control surfaces that contain the single "parent" surface node. A classical cell-centered finite volume methodology[10] is used for the 1-D virtual domains, where the discretization, storage, and numerical solutions all occur within the boundary condition implementation and only interact with the main CVFEM flow solution through fluxes and solution variables at the exposed surface.

Each 1-D domain is assumed to have a fixed geometry that is filled with a simple porous material that is allowed to react chemically to form gaseous and other solid species. Since the geometry of each discretization control volume is fixed, the porosity of each volume is assumed to increase as species are converted from solid to gas. It is assumed that the gaseous species within the pores of the solid phase are of secondary concern for mass and energy transport within the boundary, and as such no discrete transport equation is solved for them. The approximation is instead made that all gases generated within the porous material appear instantaneously at the surface of the material as a mass flux into the main fluid solution. It would be straightforward to solve additional transport equations for fluid flow within the porous material if that level of fidelity were to become necessary, as in the case of oxidative reactions where oxygen must diffuse through the exposed surface into the porous material before reactions may occur.

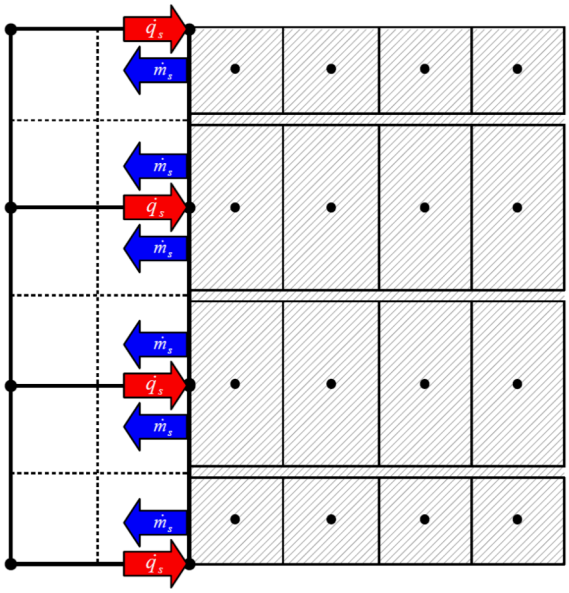

Figure 1. Representative mesh layout for 1-D composite fire boundary condition

A. Transport Equations

Within the solid phase of the porous material, simple one-dimensional transport equations for continuity, chemical species, and energy are solved in the form:

$$\frac{\partial \bar{\rho}}{\partial t} = \dot{\omega}_c''' \tag{1}$$

$$\frac{\partial \bar{\rho} Y_k}{\partial t} = \dot{\omega}_k''' \tag{2}$$

$$\bar{\rho}\bar{c}\frac{\partial T}{\partial t} = \frac{\partial}{\partial x}\left(\bar{k}\frac{\partial T}{\partial x}\right) + \dot{q}''', \tag{3}$$

where $\bar{\rho}$, $\bar{c}$, and $\bar{k}$ are the mixture-averaged bulk density, specific heat, and thermal conductivity, respectively, Y_k is the mass fraction of chemical species k, T is the temperature of the solid phase, $\dot{q}'''$ is the volumetric heat generation rate due to chemical reactions, $\dot{\omega}_k'''$ is the volumetric mass generation rate of chemical species k, and $\dot{\omega}_c'''$ is the overall mass generation rate computed as $\dot{\omega}_c''' = \sum_k \dot{\omega}_k'''$.

B. Material Models

The porous material used for this boundary condition is assumed to be of a fixed volume, i.e. there is no structural deformation allowed. The bulk density of the multi-species solid mixture is assumed to be a function of the density of each component species in their native porous state, as

$$\bar{\rho} = \left(\sum_{\mathrm{k}} \frac{Y_k}{\rho_k} \right)^{-1}, \tag{4}$$

where ρ_k is the porous density of species k, provided as a material model by the user. This model for the mixture bulk density is only used to compute the initial bulk density field, which is subsequently solved directly from Equation 1.

The porosity of the mixture is assumed to follow the model

$$\bar{\psi} = \sum_{\mathrm{k}} X_k \psi_k \tag{5}$$

where X_k is the volume fraction of species k,

$$X_k = \bar{\rho} \frac{Y_k}{\rho_k}, \tag{6}$$

and ψ_k is the porosity of pure species k, modeled as

$$\psi_k = 1 - \frac{\rho_k}{\rho_{s0,k}}, \tag{7}$$

where $\rho_{s0,k}$ is the density of the solid (non-porous) species k at a reference temperature. Note that the porosity does not appear explicitly in any of the transport equations or subsequent material models, so that it is never computed as part of the boundary condition solution. It would only appear in transport equations for the gaseous species occupying the pores of the solid skeleton, if this level of detail were ever to be added to this model.

In their most detailed form, the bulk thermal conductivity and specific heat are evaluated as a volume average and mass average of the individual species properties, respectively, as

$$\bar{k} = \sum_{\mathrm{k}} X_k k_k \tag{8}$$

$$\bar{c} = \sum_{\mathrm{k}} Y_k c_k , \tag{9}$$

although a species-independent model for the overall bulk property may be used if the individual species properties are not known.

The last quantities that require a model are the volumetric species mass production rates, $\dot{\omega}'''$, and the volumetric heat production rate, $\dot{q}'''$, which are provided by the user as part of the material model definition. These are arbitrary functions that themselves may be dependent on any of the solution variables or other material properties. If a nonreacting material is desired, then these terms may be simply set to zero.

C. Boundary Conditions

The exposed surface of the solid material interacts thermally with the environment through several mechanisms, including convective heat transfer and both radiation absorption and emission. These external fluxes must balance the conduction inside the solid material at the surface, as

$$\begin{aligned} \dot{q}'''_{\mathrm{cond}} &= \dot{q}'''_{\mathrm{conv}} + \dot{q}'''_{\mathrm{rad}} \\ &= \dot{q}'''_{\mathrm{conv}} + \epsilon \left(\dot{q}'''_{\mathrm{irrad}} - \sigma T_w^4 \right), \end{aligned} \tag{10}$$

where $\dot{q}'''_{\mathrm{cond}}$ is the conduction flux at the surface of the solid material, $\dot{q}'''_{\mathrm{conv}}$ is the convective heat flux computed in the fluid solve using the chosen methods for a convective wall that depend on the particular turbulence closure

model used, and $\dot{q}'''_{\mathrm{rad}}$ is the net radiative flux, with absorption modeled in terms of the incident irradiation on the surface and gray emission modeled in terms of the wall temperature, T_w.

On the back-side of the virtual solid material, optional convective and radiative heat transfer to a quiescent environment is modeled as

$$\begin{aligned}\dot{q}'''_{\mathrm{b}} &= \dot{q}'''_{\mathrm{b,conv}} + \dot{q}'''_{\mathrm{b,rad}} \\ &= h_c(T_N - T_{\mathrm{ref}}) + \sigma\epsilon_b(T_N^4 - T_{\mathrm{ref}}^4)\,,\end{aligned} \tag{11}$$

where h_c is a user-specified convection coefficient, ϵ_b is a user-specified back-side emissivity, T_{ref} is the modeled ambient environment temperature, and T_N is the temperature of the solution node closest to the back-side surface, assumed to be equal to the back-side surface temperature itself.

D. Numerical Implementation

A segregated, implicit solution technique is used to numerically integrate Equations 1–3. The discretized form of the continuity equation, Equation 1, is derived by first integrating it over the finite volume V and the time step Δt to yield

$$\int_{\Delta t}\left[\int_V \frac{\partial \bar{\rho}}{\partial t}\mathrm{dV} - \int_V \dot{\omega}'''_{\mathrm{c}}\,\mathrm{d}V\right]dt = 0 \tag{12}$$

$$\int_{\Delta t}\left[V_i\frac{\partial \bar{\rho}_i}{\partial t} - V_i\dot{\omega}'''_{\mathrm{c,i}}\right]dt = 0\,. \tag{13}$$

Discretizing the temporal derivative using a first-order backward difference approximation and solving for the bulk density at the new time step yields

$$V_i\,(\bar{\rho}_i^{n+1} - \bar{\rho}_i^{n}) - V_i\,\dot{\omega}'''_{\mathrm{c,i}}\,\Delta t = 0 \tag{12}$$

$$\bar{\rho}_i^{n+1} = \bar{\rho}_i^{n} + \dot{\omega}'''_{\mathrm{c,i}}\,\Delta t\,. \tag{13}$$

Note that this equation is linearized by evaluating the source term at the most recent estimate of the solution state at time level $(n+1)$.

The species transport equations, Equation 2, undergoes an identical transformation to yield the closed-form solution

$$Y_{k,i}^{n+1} = \frac{\bar{\rho}_i^{n}Y_{k,i}^{n} + \dot{\omega}'''_{\mathrm{k,i}}\,\Delta t}{\bar{\rho}_i^{n+1}}\,, \tag{14}$$

where the bulk density at the new time level is used from Equation 13, and the source term is evaluated from the most recent estimate of the solution state at time level $(n+1)$.

The energy equation also undergoes a similar transformation, but with added complexity due to the inclusion of spatial derivatives. Equation 3 is first integrated in both space and time, and the Gauss divergence theorem is used to remove one level of spatial derivatives in the diffusive flux term, yielding

$$\int_{\Delta t}\left[\int_V \bar{\rho}\bar{c}\frac{\partial T}{\partial t}\,dV - \int_A n\cdot\left(\bar{k}\,\frac{\partial T}{\partial x}\right)\mathrm{d}A - \int_V \dot{q}'''\,dV\right]dt = 0 \tag{15}$$

Integrating numerically in space yields

$$\int_{\Delta t}\left[\,\bar{\rho}_i\bar{c}_iV_i\,\frac{\partial T_i}{\partial t} + A_{i-\frac{1}{2}}\,\bar{k}_{i-\frac{1}{2}}\left(\frac{T_i - T_{i-1}}{\Delta x_{i-\frac{1}{2}}}\right) - A_{i+\frac{1}{2}}\bar{k}_{i+\frac{1}{2}}\left(\frac{T_{i+1} - T_i}{\Delta x_{i+\frac{1}{2}}}\right) - \dot{q}_i'''V_i\right]dt = 0\,, \tag{16}$$

where the $\left(i+\frac{1}{2}\right)$ and $\left(i-\frac{1}{2}\right)$ subscripts indicate quantities at the high and low control volume boundaries, respectively. Integrating in time and linearizing the equation by evaluating the coefficients at the most recent estimate of the $(n+1)$ solution state yields

$$\bar{\rho}_i \bar{c}_i V_i \left(\frac{T_i^{n+1} - T_i^n}{\Delta t}\right) + A_{i-\frac{1}{2}} \bar{k}_{i-\frac{1}{2}} \left(\frac{T_i^{n+1} - T_{i-1}^{n+1}}{\Delta x_{i-\frac{1}{2}}}\right) - A_{i+\frac{1}{2}} \bar{k}_{i+\frac{1}{2}} \left(\frac{T_{i+1}^{n+1} - T_i^{n+1}}{\Delta x_{i+\frac{1}{2}}}\right) - \dot{q}_i''' V_i = 0\,. \tag{17}$$

This leads to a tridiagonal system of coupled linear equations for the temperature at time level $(n+1)$, which is solved using a direct method with the DGTSL module of the SLATEC library.

The continuity, species, and energy equations are solved sequentially in the order described, and the solution is repeated until the maximum normalized change in the temperature solution,

$$T_{\text{err}} = \frac{|T^{n+1} - T^*|}{T^{n+1}}, \tag{18}$$

satisfies the user-specified tolerance, where T^* is the solution from the previous iteration.

III. Verification

It is good practice to verify any model implemented in a CFD code. Verification is generally understood to be the process whereby one ascertains that the theory that was designed for implementation was indeed implemented as prescribed[11,12]. Verification can take many forms, however high quality verification is able to provide high confidence in the model implementation, and also makes a good unit test for regularly testing the continued acceptability of advancing code versions stored in a code repository. Methods of manufactured solution, or analytical solutions represent some of the better ways to verify an implementation. The comparative simplicity of the surface model lends itself to quality verification processes.

A. 1-D Semi-Infinite Transient Heat Transport

Because the theoretical model is one-dimensional, there are several options for quality verification. Closed-form solutions exist for several problems of this type. One that makes a lot of sense is for a constant surface heat flux on a semi-infinite homogeneous slab. Incropera and Dewitt (1990)[13] give the solution to this scenario as:

$$T(x,t) = T_i + \frac{2q''_o(\alpha t/\pi)^{1/2}}{k} \exp\left(\frac{-x^2}{4\alpha t}\right) - \frac{q''_o x}{k} \operatorname{erfc}\left(\frac{x}{2\sqrt{\alpha t}}\right) \tag{19}$$

Here T is the temperature, which is a function of the distance inside the surface x and time t. The temperature is a function of the initial temperature, T_i, the constant absorbed flux q''_o, the thermal diffusivity α, and the thermal conductivity k. Here 'erfc' is the conjugate Gaussian error function (the Gaussian error function subtracted from unity). Thermal properties were the same as used for the subsequent analysis, and represent approximate thermal properties for PMMA as extracted from the literature. These are described in Table 1.

Table 1. Thermal properties for PMMA used in this study

Property	units	value
Solid Density	kg/m^3	1190
Solid Specific Heat	J/kgK	860.7
Solid Conductivity	W/mK	0.1
Emissivity	-	1.0
Thermal Diffusivity	m^2/s	9.76E-8
$T_{initial}$	K	300

Fluid properties were computed automatically in the gas phase using a Cantera algorithm from gas phase curve fits in the standard NASA representation out of a standard molecular data repository.

B. Verification Conditions

To verify that the fluxes from the fluid side of the calculation are appropriately mapped and transported to the boundary nodes, two simple cases are simulated. One is a convection-dominant scenario, and the other a radiation-dominant scenario. Both of these were calculated with the coarse mesh later presented for the sensitivity analysis study. Modifications were made to achieve a radiation- and convection-dominant flow, and to achieve a nearly constant absorbed flux. The radiation-dominant flow is achieved by reducing the ambient gas density by a factor of 10, and reducing the emissivity to a very low value. The convection dominant flow is achieved by setting the radiation boundaries to a transparent condition and a high temperature inflow, as well as a low emissivity on the surface. The convection condition was more difficult to maintain constant, as the surfaces that heat up will change the boundary layer temperatures with time. The boundary conditions were slightly different for the analytical calculations compared with the model predictions, the differences reflecting the reality of the scenario modeled. The mean incident flux over 50 seconds from the prediction was used as the input to the closed form analytical solution. Figure 2 shows the comparison between the analytic and simulated flux, suggesting good implementation.

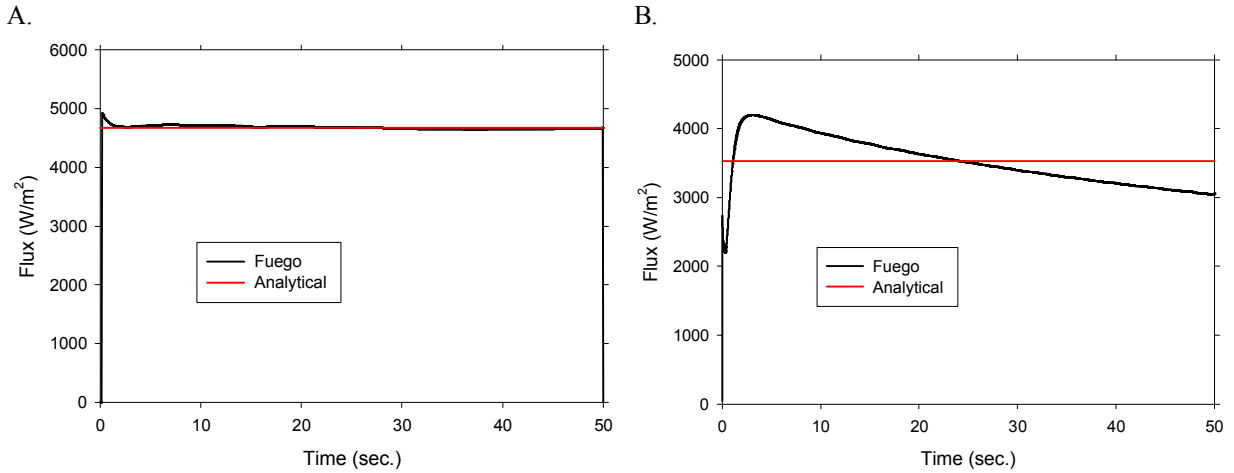

Figure 2. Predicted versus analytical (average) net (absorbed) flux used for verification of a radiation (A) and convection (B) dominant flux scenario.

C. Verification Comparisons

Figure 3 shows the predictions from Fuego compared to the analytical results. The simulation results are plotted as points, whereas the analytical solution is plotted as lines. This is done for the first five finite element nodes for the simulation, with corresponding predictions from the analytical model. For the radiation dominated scenario, the fluxes were very close, and the predictions are nearly indistinguishable. For the convection dominant scenario, the results deviate slightly, as would be expected based on the difference in the transient boundary condition. Nodes are 1 mm thick, with node centers at the center of the node (thus Node 1 in Fig. 3 is at 0.5 mm, Node 2 at 1.5 mm, etc.).

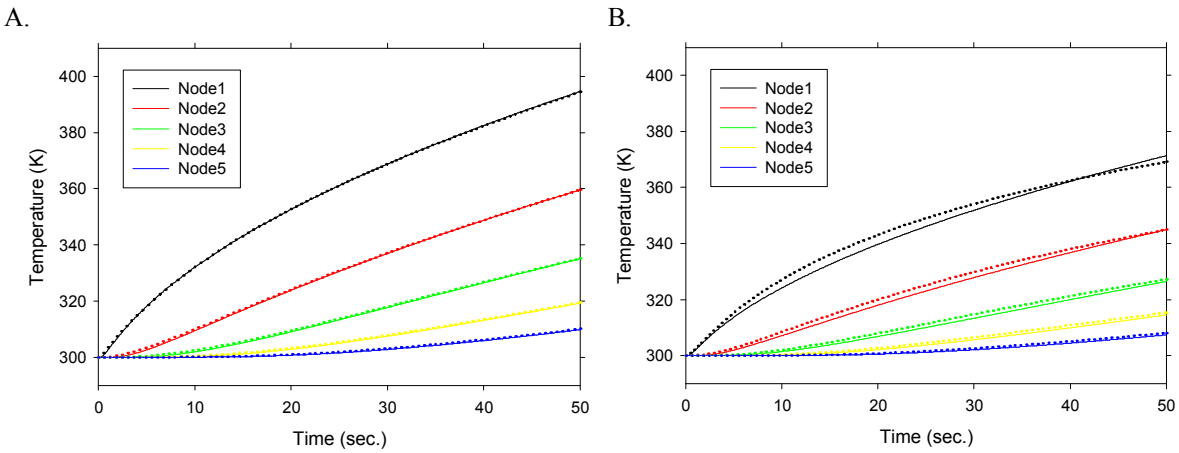

Figure 3. Model predictions of temperature at consistent points through the conducting solid for a radiation (A) and convection (B) dominated flow. Lines represent analytical model predictions, and dotted lines are the numerical predictions for a convection dominant scenario.

IV. Sensitivity Study Results

As an initial test of this capability, a good test case was desirable. A literature search commenced to find a scenario to use as a base test case. These experimental conditions were selected first by determining that the use of PMMA as a fuel makes a good simple case for initial comparisons. There are many reports on the burning of this material, and physical properties are generally available. After reviewing other PMMA burn experimental efforts, the down-selection criteria that were most important were that the tests that were well documented, and more amenable to replication with the simulation tool. The work of Ndubizu et al (2005)[7] is used as the context for this effort. They performed tests in which a slab of PMMA was radiatively ignited in a calm wind environment. Once the material was on fire, they moved the material in front of a prescribed wind.

A cursory study of some of the input parameters was performed for this work. The variation of several of the input parameters was examined, as well as mesh resolution. Table 2 shows the specific parameters that were varied as part of this study. Besides mesh resolution, the timestep was varied by changing the peak allowed Courant Friedrichs Lewy (CFL) number for the calculations. The 'compres' variable is the resolution through the solid, with a higher number representing a greater discretization of the fuel depth. The 'E' variable is the activation energy, which is varied by 5%. The 'den' variation is the solid material density. The 'emis' variation is the solid emissivity, which is also varied by 5%. Each of the variations is performed on the medium mesh.

Table 2. The simulation matrix

Case	Mesh Length Scale Resolution Relative to Coarse	Nodes	Nominal Parameter	Parameter Variation
coarse	1	16K		
med	2	118K		
fine	3	389K		
xfine	4	908K		
med_CFL	2	118K	CFL=2	CFL=1
med_compres	2	118K	Solid Node Count = 10	Solid Node Count = 20
med_E	2	118K	Activation energy = 160.6 kJ/mol	Activation Energy*1.05
med_den	2	118K	Density = 1190 kg/m^3	Density*1.05
med_emis	2	118K	emissivity = 0.95	emissivity*1.05

A. Simulation Details

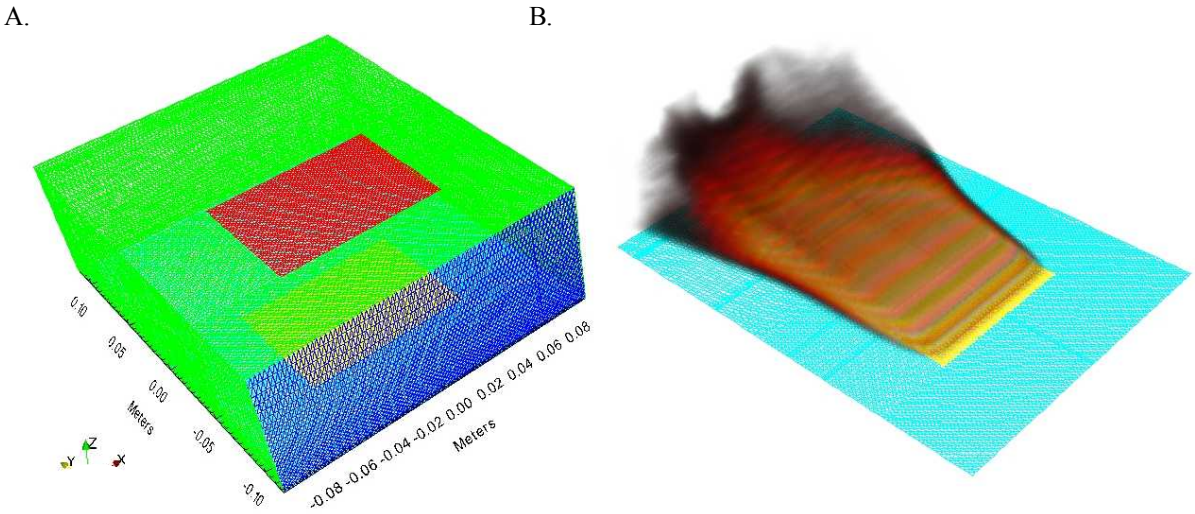

Figure 4. An illustration of the coarse mesh (A) with dimensions, and the predicted fire (B) using a volume rendering scheme to represent the fire at a mature time.

The scenario was constructed using a rectangular domain of 0.075 m high, 0.19 m wide, and 0.235 cm long A 10 x 8.5 x 5 cm slab of PMMA was assumed in a 84 cm/s cross-wind. This is represented by the yellow mesh in Fig. 4, which shows the full mesh and a volume rendering of the predicted fire. The inflow boundary (dark blue color) was a Dirichlet velocity condition. The open boundary (green color) was set with ambient conditions. The aluminum base was also modeled as a 1-D conductive material with textbook properties of aluminum (light blue color).

Because the exact details of the ignition were not presented in the technical report, a time varying velocity and ignition panel environment was created to approximate what might have been the real environment. The radiating panel (red color in Fig. 4) was the same dimensions as the PMMA sample, and was radiating at 1400 K initially. At 50 seconds, this decreased to 400 K. The air flow was initially zero, and ramped slightly to 0.1 m/s between zero and 30 seconds. It then ramped quickly to the nominal 0.84 m/s flow rate. The assumed radiative panel and wind velocity profiles are plotted in Fig. 5.

Fuel was assumed to be methane, which is used as a surrogate to the more complex product species expected from the pyrolysis of PMMA.

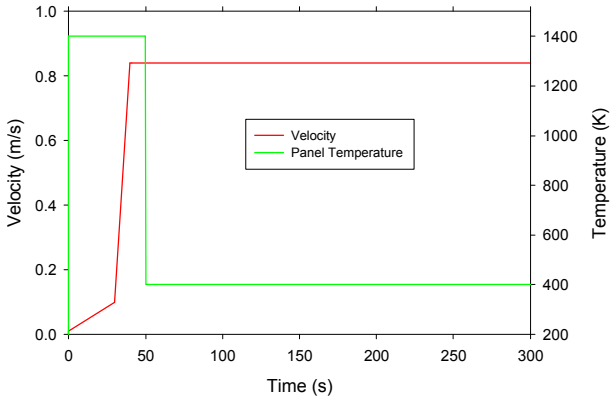

Figure 5. Transient assumed boundary conditions for the radiative heater and the air in-flow.

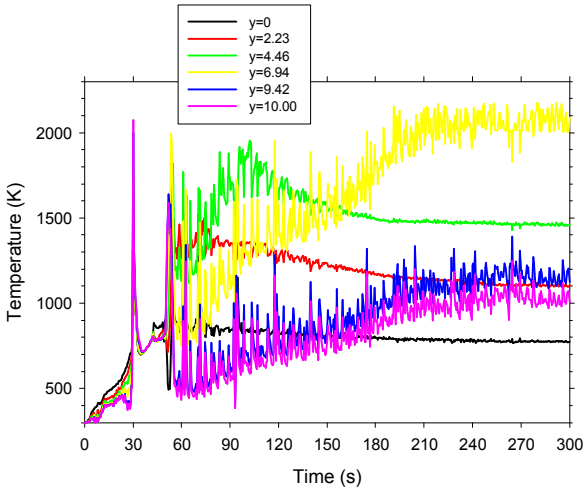

Figure 6. Predicted gas temperatures 35 mm downstream of the leading edge of the fire at the centerline varying in elevation (y).

B. Data Comparison

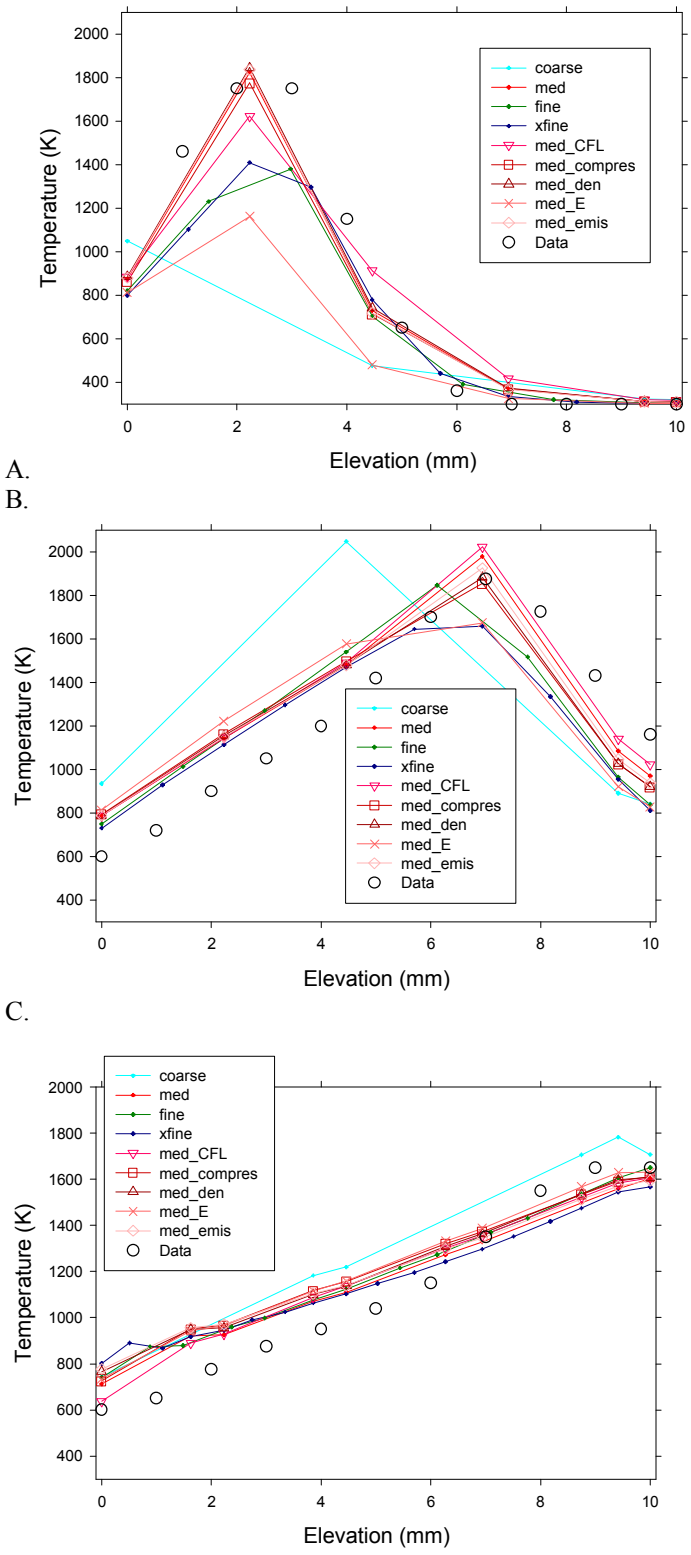

Figure 7. Predicted gas temperatures compared to the measured thermocouple temperatures at 10 (A), 35 (B), and 76 (C) mm downstream of the leading edge.

To make validation assessments, it would be desirable to have better details of the ignition process. It would also be desirable to have higher quality input data to the model for the fuel and material properties. This point is made more clear examining Fig. 6 results, which show the time varying predicted centerline temperature at 35 mm downstream of the leading edge of the flame for several elevations. The plot shows that even after the boundary condition steady state condition is reached at 60 seconds, the developed flame above the fuel is still transient until about 210 seconds. The test report indicates that the temperature measurements presented correspond to measurements at a specific time. If we use our same time, the comparisons are not particularly good. However, if we use the more mature data (210 seconds and beyond), our predictions match the data from the test on a qualitative basis. Since the post-ignition time is not indicated, it is conjectured that the experimental data better correspond to the more mature simulation times.

Since the effort here is focused on parameter sensitivity, it is appropriate to at least demonstrate that the model approximates the environment. For the most part, all meshes reproduce the thermocouple measurements in the gas temperature predictions, as can be seen in Figs 7A-7C, which show comparisons with data in the steady-state regime (210 seconds and beyond). Introduced in this plot is a color scheme that will be used in subsequent plots. The color indicates the mesh type, while shades of red are coordinated to the parameter varied for the sensitivity analysis. The coarse mesh did not have sufficient resolution to accurately reproduce the data peaks.

Because the predictions provide detailed data, it was possible to extract the components of the incident flux to the surface as a function of distance downstream. Results from three mesh resolutions are plotted in Fig. 8. The model predictions suggest that the flame at the leading edge is almost entirely driven by convective heat flux. At around 55 mm downstream, the convective component to the total flux is equal to that of the radiative flux. The radiative flux is initially low, but increases to become the dominant component to the total

flux after about 55 mm. The total flux decreases slightly progressing downstream. This is consistent with erosion patterns noted by Ndubizu et al.[7], which showed the material near the leading edge decomposing more than the material further down-stream, although they did not indicate the convective or radiative nature of the surface flux.

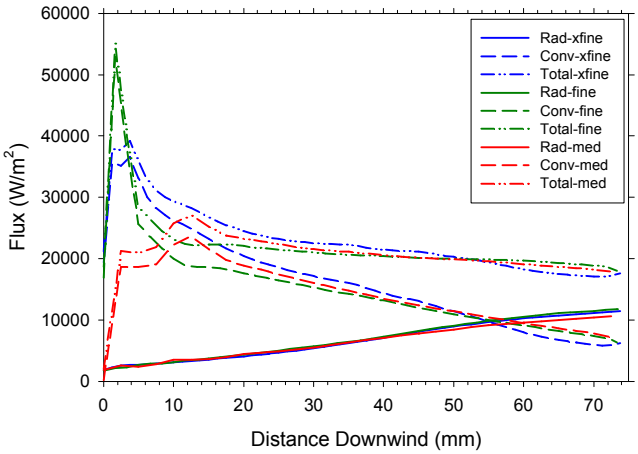

Figure 8. Predicted mass loss rate for the simulation scenarios.

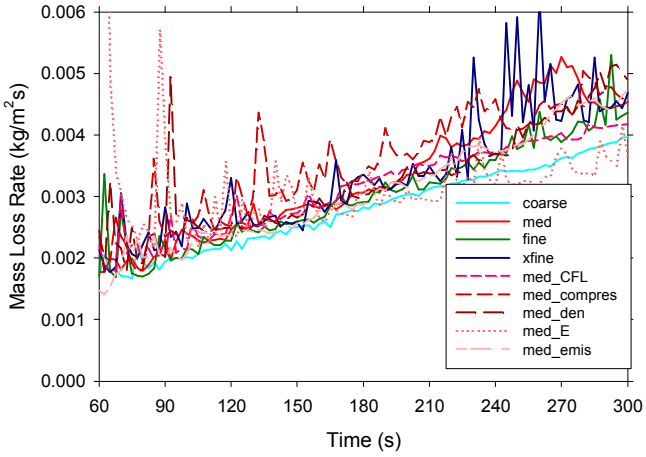

Figure 9. Predicted mass loss rate for the simulation scenarios.

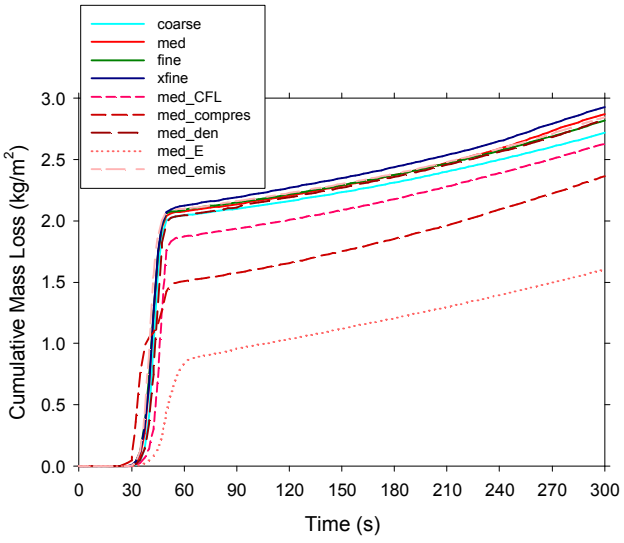

Figure 10. Cumulative mass loss for the simulation scenarios.

C. Sensitivity Analysis

Some indications of the effects of the various parameters are evident in preceeding figures. The metric of interest for this analysis is the mass loss rate. Instantaneous burn rate predictions are found in Fig. 9. This plot shows data from 60 seconds to 300 seconds, and shows the time varying burn rates for the various parameter choices. It indicates that all parameter variations suggest the burn rate steadily increases with time from about 0.02 kg/m^{2}s at 60 seconds to 4.5 kg/m^{2}s at 300 seconds. Examination of the data suggests the coarse case as an outlier, with slightly lower mass loss rate than the rest of the cases. The med_E case that involves a 5% variation in the activation energy is also lower than most of the other predictions at later times. This is because increasing the activation energy delays the solid decomposition.

A cumulative mass loss plot is found in Fig. 10. This plot exhibits more clearly the effect of the sensitivity parameters on the initial transient, as well as the steady burn. The transient behavior is not nearly as evident, as the fluctuations are much smaller on a cumulative plot. The cumulative mass loss plot also suggests the reason for which the predictions from earlier times were eliminated from the mass loss rate plot. At ignition, there is a large initial burn rate. After the local oxygen is consumed and the radiant panel shut off, the burn rate settles to a more steady burn rate. This initial transient is mostly the same for all the cases, except there are three cases that are outliers. The med_E case ignited slower, and consumed much less material than the other cases during this initial ignition period. This is not surprising, as an increase in activation energy would require more energy to ignite the PMMA. The med_compres case is also low compared to the majority of other scenarios. This scenario peaks earlier than the others, as indicated by an earlier initial rise. But the total mass lost in the early phase is lower. This indicates that the near-surface resolution of the solid material allows for earlier ignition, but that the surface resolution

inhibits heating in the first sub-layer, which slows the reactions quicker than they would occur with a coarser surface mesh. This suggests some subtle differences might be noted if the solid material resolution is insufficiently high. The other outlier in this plot is the med_CFL scenario. This suggests the timestep needs to be small to resolve the initial transient. The coarse mesh diverges slightly (slower burn at later time) from the main grouping of the rest of the scenarios. Other variations are comparatively small.

The average mass loss rate for two time ranges is found plotted in Fig. 11. This plot allows for improved evaluation of the burn rate through the steady burn period following the initial transient. Outliers in this plot are the coarse scenario, which has the lowest mass loss rates over the intervals, and the med_compres scenario, which has the highest.

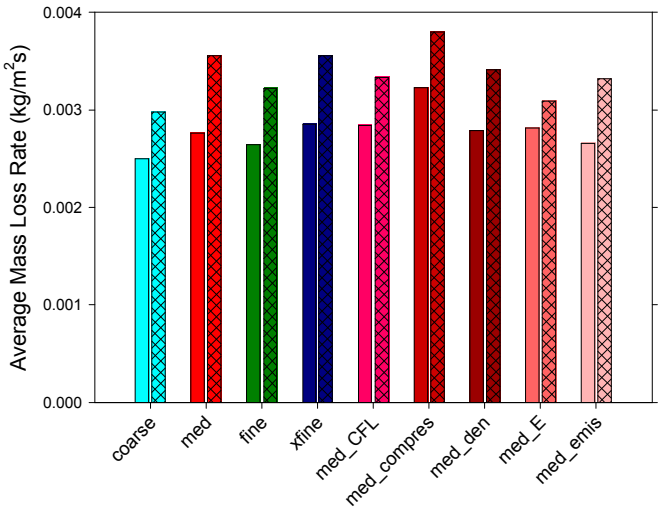

Figure 11. Average mass loss rate over the 100-200 second interval (no hatching) and 100-300 second interval (hatched).

V. General Discussion

The theory and implementation of a 1-D combustion model is presented and verified in earlier sections. The verification was performed for both convective and radiative fluxes, which helps provide confidence in the boundary condition at the surface. Furthermore, the scenario that was verified is a full 3-D calculation, which provides confidence in the implementation for practical scenarios (i.e. as the capability is normally expected to be used). The verification might have been performed at less than practical conditions, in which case the adequacy in this regard would need to be inferred through extrapolation.

The scenario that was selected for analysis turned out to be an excellent scenario for exploring the dynamics of the incident flux. The transition between radiative and convective dominated heating of the PMMA surface at around 55 mm downwind is suggestive of the importance of both of these mechanisms to the burn rate of a solid surface at these length scales. Evident from the experimental work is the importance of the length scale above the burning surface. Fig. 7A shows the peak temperature at about 2 mm above the surface 10 mm downstream of the leading edge of the burning sheet of PMMA. Consider now the more practical scale problem of a burning room or building. The scenario simulated in this effort may be a component of a larger scale fire. To accurately represent the burning or combustion of a material of this type in that environment, the spatial resolution needs to be in the millimeter range for accurate resolution of the dynamics. Such uniform resolution is not practically solved. One can circumvent this issue by using local refinement, or by employing sub-grid models that are tuned to be able to predict these dynamics without fully resolving the boundary layer of the fire.

The sensitivity analysis was a helpful exercise for evaluating the sensitivity to the various numerical parameters in this problem. The mesh resolution was generally not a major factor once sufficient resolution was used. The coarse scenario mass loss rates were different than those of the other four resolutions evaluated. Figure 7A most clearly suggests the primary reason for this difference. The mesh resolution was inadequate at the toe of the fire to resolve the flame at 2 mm above the surface. The resolution is close to being insufficient to sustain active burning, and presumably with a slightly higher wind speed the fire blows out for the coarse resolution case. Evaluating this scenario with steadily increasing wind speeds might be informative, and could help quantify the propensity for blow-out as a function of resolution. More to the point, this observation suggests the need for something else in the model to capture the near-surface dynamics if the coarser resolutions are to be used with any expectation of accuracy. The coarse mesh was resolved to 5 mm, which is incredibly fine for many practical scaled problems.

It is important to observe that the flame at the toe results in a convective dominant flux at that point on the surface of the burning PMMA. Practical scaled fires normally consist of many fuel sources, and often are radiation dominant systems. Because this scenario is a simple scenario with a single heat source (the PMMA), the dynamics are increasingly sensitive to this parameter. In a larger fire, the radiation can be fully dominant, so the sensitivity found in this analysis might be much lower for larger-scale and more practical scenarios.

Examining the other parameters in the sensitivity analysis, there are further findings to be discussed. First, the resolution through the combustible material was found to be sensitive both in the ignition phase and in the more steady-state burn time. It resulted in an earlier ignition, but with less mass loss through the transient start-up. Through the steady burn period, the mass loss was slightly higher than the other scenarios. Because this parameter exhibited moderate effect through both periods, this parameter can be considered the one to which the model is most sensitive. Because this parameter exhibited sensitivity, it is worthwhile to consider improvements. A mesh biasing that allocates higher resolution near the interface might help reduce the resolution requirements without significantly affecting the quality of the prediction. One would want to maintain the high resolution at the solid/gas interface as the surface recedes. Such a model would be valuable, and help improve the efficiency of the model in this regard.

The timestep was found to be a small factor, most evident in the early transient. This study would benefit from a subsequent decrease in timestep to demonstrate adequate convergence in this regard. This was not completed for this study, but merits attention in the future.

The activation energy was found to result in very high sensitive to a 5% change during the early transient. This was not particularly surprising, as the activation energy is in the exponent of the kinetic rate expression. Despite a large sensitivity found in the early transient, the 100-200 second average mass loss rate was reasonably close to the other scenario predictions. The 100-300 second average was also reasonably close, but the growth rate is a little smaller than for the other scenarios. This suggests that this parameter is of high sensitivity. It was perhaps misleading to vary this parameter alone at a 5% level. The pre-exponential factor is normally fit in concert with the activation energy, so a small change in the activation energy can result in a large change in the actual rate predictions if the pre-exponential value is not adjusted in concert to fit the data at the centroid temperatures at which the model was formed and is being used. Regardless of this fact, the parameter was shown to be highly sensitive, and thus should be a focus of accurate data input.

The density and emissivity parameters were never found to be particularly sensitive to the 5% change imposed in this study. Density was varied as a surrogate for conductivity and specific heat, as all three of these are components of the thermal diffusivity. These parameters will certainly exhibit sensitivity for higher values. At the 5% accuracy, their effect was smaller than the other parameters in this study during the early transient and the more steady longer-term predictions. The other parameters therefore merit more attention in future work.

VI. Conclusion

We present a boundary model for the 1-dimensional behavior of a combustible solid. The implementation of the model is shown through a verification exercise to adequately reproduce the analytical solution to of heat transport through a semi-infinite solid.

The model was demonstrated in the context of a set of experiments documented in the literature that describe the burning of a slab of PMMA (Plexiglas). The general shape of the flame was similar to that from the literature, as inferred from a comparison of predicted gas temperatures to experimental thermocouple temperature measurements.

A sensitivity analysis suggests the importance of several model parameters to the quantitative prediction results. Results were sensitive to the 5% variation in the activation energy. At 5% variation, solid density and emissivity were not found to be significant variables to the mass loss predictions. At the coarse level (~5 mm resolution), the mesh was important, but at finer levels it was less so. Other discretization parameters also showed moderate sensitivity.

For practical scale fire simulations, one would require a prohibitively high level of refinement to resolve the dynamics in this problem. Thus, it is advisable that a modified sub-grid model for boundary layer combustion be considered to increase the tractability of larger scale scenario predictions.

Acknowledgments

Sandia is a multiprogram laboratory operated by Sandia Corporation, a Lockheed Martin Company, for the United States Department of Energy under Contract No. DE-AC04-94AL85000. Work was funded through the ASC program. Reviews by Randy Watkins, Sean Kearney and Amanda Dodd are appreciated. Diane Mendiola helped transcribe the equations in preparation for publication.

References

[1.] H.Y. Wang, P. Joulain, J.M. Most, “Modeling on burning of large-scale vertical parallel surfaces with fire-induced flow,” Fire Safety Journal 32, 241-271, 1999.

2. Consalvi, J.L., Y. Pizzo, A. Kaiss, J.L. Torero, B Portiere, "A theoretical and numerical evaluation of the steady-state burning rate of vertically oriented PMMA slabs," Combustion Theory and Modelling, 12:3, 451-475, 2008.

3. Novozhilov, V., D.J.E. Harvie, A.R. Green, J.H. Kent, "A Computational Fluid Dynamic Model of Fire Burning Rate and Extinction by water Sprinkler," Combustion Science and Technology, 123:1-6, 227-245, 1997.

4. Ananth, R., C.C. Ndubizu, and P.A. Tatem, "Burning rate distributions for boundary layer flow combustion of a PMMA plate in forced flow," Combustion and Flame, 135, 35-55, 2003.

5. Hebert, D., A. Coppalle, and M. Talbaut, "2D soot concentration and burning rate of a vertical PMMA slab using Laser-Induced Incandescence," Proceedings of the Combustion Institute, 34, 2575-2582, 2013.

6. Fereres, S., C. Lautenberger, A.C. Fernandez-Pello, D.L. Urban, and G.A. Ruff, "Understanding ambient pressure effects on piloted ignition through numerical modeling," Combustion and Flame, 159, 3544-3553, 2012.

7. Ndubizu, C.C., R. Ananth, P.A. Tatem, "Transient burning rate of a noncharring plate under a forced flow boundary layer flame," Combustion and Flame, 141, 131-148, 2005.

8. Baliga, B. R. and Patankar, S. V., "A Control Volume Finite-Element Method for Two-Dimensional Fluid Flow and Heat Transfer," *Numerical Heat Transfer*, 6(3):245-261, 1983.

9. Schneider, G. E. and Raw, M.J., "A Skewed, Positive Influence Coefficient Upwinding Procedure for Control-Volume-Based Finite-Element Convection-Diffusion Computation," *Numerical Heat Transfer*, 9(1):1-26, 1986.

10. Versteeg, H.K. and Malalasekera, W., An Introduction to Computational Fluid Dynamics – The Finite Volume Method, Second Edition, Pearson Education Limited, 2007.

11. AIAA, *Guide for the Verification and Validation of Computational Fluid Dynamics Simulations*, AIAA G-077-1998

12. Oberkampf, W.L., and Trucano, T.G., "Verification and Validation in Computational Fluid Dynamics," Sandia Report SAND2002-0529, March 2002.

13. Incropera, F.P. and DeWitt, D.P., Introduction to Heat Transfer Second Edition, John Wiley & Sons, 1990.